

Passive Acoustic Mapping using Data-Adaptive Beamforming Based on Higher-Order Statistics

Erasmia Lyka, Christian M. Coviello, *Member, IEEE*, Catherine Paverd, Michael D. Gray, and Constantin-C. Coussios

Abstract— Sources of nonlinear acoustic emissions, particularly those associated with cavitation activity, play a key role in the safety and efficacy of current and emerging therapeutic ultrasound applications, such as oncological drug delivery, blood-brain barrier opening and histotripsy. Passive Acoustic Mapping (PAM) is the first technique to enable real-time and non-invasive imaging of cavitation activity during therapeutic ultrasound exposure, through the recording and passive beamforming of broadband acoustic emissions using an array of ultrasound detectors. Initial limitations in PAM spatial resolution led to the adoption of optimal data-adaptive beamforming algorithms, such as the Robust Capon Beamformer (RCB), that provide improved interference suppression and calibration error mitigation compared to non-adaptive beamformers. However, such approaches are restricted by the assumption that the recorded signals have a Gaussian distribution. To overcome this limitation and further improve the source resolvability of PAM, we propose a new beamforming approach termed Robust Beamforming by Linear Programming (RLPB). Along with the variance, this optimization-based method uses higher-order-statistics of the recorded signals, making no prior assumption on the statistical distribution of the acoustic signals. RLPB is found via numerical simulations to improve resolvability over TEA and RCB. In vitro experimentation yielded improved resolvability with respect to the source-to-array distance on the order of 22% axially and 13% transversely relative to RCB, whilst successfully accounting for array calibration errors. The improved resolution and decreased dependence on accurate calibration of RLPB is expected to facilitate the clinical translation of PAM for diagnostic, including super-resolution, and therapeutic ultrasound applications.

Index Terms— Image-guided treatment, optimization, quantification and estimation, ultrasound

I. INTRODUCTION

A growing number of non-invasive ultrasound therapies exploiting both thermal and mechanical bioeffects are currently in clinical trials or in increasingly widespread clinical use. Examples of such emerging applications are

thermal ablation of tumours [1] or uterine fibroids [2]–[4], lithotripsy of kidney stones [5], ultrasound-mediated drug delivery for cancer treatment and gene therapy [6]–[8], sonothrombolysis for stroke treatment [9], brain ablation for treatment of essential tremor [10], and opening of the blood-brain barrier for treatment of brain tumors [11], [12].

Monitoring of ultrasound therapies, though, remains a key challenge, common across all therapeutic ultrasound applications that should be addressed depending on the mechanisms involved. Among the available modalities, the only two currently clinically approved methods are MRI, which is particularly well-suited for monitoring thermal treatments, and active ultrasound B-mode imaging, best suited to monitoring thermal therapies leading to large boiling bubbles [13] or cavitation-based therapies resulting in permanent hyperecho change [14]. However, there is a lack of an established modality for reliable localization of sources of cavitation, as well as classification and quantification of their activity. Considering cavitation as the key mechanism behind multiple emerging ultrasound applications, such as ultrasound-mediated blood-brain barrier opening and drug delivery, which are not intended to result in permanent tissue damage, introducing such a monitoring method would improve the safety and efficacy of these applications, and facilitate their clinical adoption.

Passive Acoustic Mapping (PAM) has been introduced to fill the aforementioned gap [15]–[17]. It is based on passively (i.e. without requiring an active interrogating pulse) recording the acoustic emissions originating from a region of interest using an ultrasound array. The center frequency of the array is typically 7-10 times higher than the therapeutic ultrasound, particularly when aiming at detecting broadband acoustic emissions associated with inertial cavitation. Filtering of the recorded acoustic emissions for signal-of-interest isolation, and combination of the filtered signals from all detectors using beamforming techniques provides maps of the source energy distribution within a pre-defined region of interest over a specified time period. PAM does not suffer from interference issues, despite being concurrent with the therapeutic pulse, since it does not require a transmitting pulse for monitoring purposes. PAM has already been applied in the fields of HIFU ablation [13], [18]–[20], ultrasound-mediated drug delivery [21]–[23], transcranial ultrasound treatments [19], [24], and histotripsy [25], indicating its potential to be used both as a stand-alone monitoring method, and in combination with either MRI or B-mode imaging. Additionally, PAM, in combination with super-resolution techniques, has been applied as a purely diagnostic modality for high-resolution vascular imaging [26]. Such an application demonstrates the versatility and

This work was supported by the Engineering and Physical Sciences Research Council (EPSRC) under grant number EP/K020757/1, and EPSRC Departmental (DTA) studentship (E. Lyka).

E. Lyka, M.Gray, C. Paverd, and C.-C. Coussios are with the Institute of Biomedical Engineering, Department of Engineering Science, University of Oxford, Oxford, UK (e-mail: constantin.coussios@eng.ox.ac.uk).

C. M. Coviello was with the Institute of Biomedical Engineering, Department of Engineering Science, University of Oxford, Oxford, UK. He is now with Oxsonics Ltd, Oxford, UK.

Copyright (c) 2017 IEEE. Personal use of this material is permitted. However, permission to use this material for any other purposes must be obtained from the IEEE by sending a request to pubpermissions@ieee.org.

potential of this mapping technique.

Clinical adoption of PAM is presently hindered by a number of challenges. Ultrasound therapy monitoring using conventional arrays is often done at long axial stand-off distances between a region-of-interest and the array due to setup and acoustic access. Additionally, restrictions on the array aperture size will limit the passive algorithm source resolvability, especially in the axial direction with respect to the array of detectors [17], [27]. Several beamforming approaches have been proposed, either in the time or frequency domain [16], [17], [27]–[30], classified into non-adaptive and data-adaptive methods. This classification implies that for a data-adaptive beamformer the signals recorded by all elements have a direct impact on the way they are combined in order for the source energy originating from a certain location to be estimated. Data-adaptive beamformers are expected to be more computationally demanding, but potentially more effective in mitigating errors arising from variability in the geometric arrangement or sensitivity of the receiving array of sensors compared to non-adaptive beamformers.

An example of a non-adaptive beamformer is Time Exposure Acoustics (TEA) [17], [31], which estimates source energy at a location of interest by the cross-correlation of all recorded signals, pre-steered and amplitude compensated for this specific location. As far as data-adaptive beamforming algorithms are concerned, the Capon Beamformer (CB) [32] and the Robust Capon Beamformer (RCB) [33], [34] have been proposed in the context of PAM [27]. Both methods optimize a set of weights for the sensors, attempting to reduce artifacts due to interference, including that created by reverberations of acoustic emissions between multiple bubbles [27]. RCB outperforms CB, as it accounts for array imperfections, such as calibration or element positions errors. This is achieved by introducing a region of uncertainty that allows the steering vector (i.e. the vector that steers the signals of the array as if they originate from a certain location/direction) to vary within this region, resulting in compensation for errors in array configuration.

Replacement of TEA with RCB resulted in significant artifact suppression and improved spatial resolution, allowing simultaneously for calibration error mitigation [27]. However, there is a compromise that needs to be made between interference suppression capability and mitigation of calibration errors, determined by the choice of the size of the uncertainty region. Additionally, RCB assumes that the signals of interest follow a Gaussian distribution. This assumption arises from the fact that the weight calculation in RCB is based on the minimization of the variance of the array output. In statistical terms, in minimizing the variance of a signal, only the second-order statistics of the signal are taken into consideration. It is, therefore, assumed that the higher order statistics (HOS) of the signals are zero, which may not always be valid for signals passively received during ultrasound therapy.

There has already been considerable research in biomedical signal processing based on the HOS of the signals [35]. Several beamformers based on HOS have been proposed in the optimum array processing literature. Adaptive beamforming based on HOS has been attempted in the field of far-field speech recognition using kurtosis or

negentropy maximization, achieving efficient noise and reverberation suppression [36], [37]. A polyspectra approach has also been proposed for source detection and parameter estimation of wideband sources demonstrating optimal performance for non-Gaussian signals in the presence of additive Gaussian noise [38]. Additionally, a linearly-constrained minimum variance beamformer reformulated for non-Gaussian probability density distributions has been proposed for brain activity localization from magnetoencephalographic (MEG) data [39].

To date, none of these novel approaches have been applied to mapping of ultrasound sources of non-linearity, including cavitating bubbles. Several reasons could potentially be identified as to why HOS analysis of the cavitation signals could be proven beneficial. Inertial cavitation is observed to be dominated by broadband acoustic emissions, but there are few reasons that could be identified why these emissions may not fall exactly within a Gaussian distribution. Firstly, the use of pre-formed bubbles, either in the form of ultrasound contrast agents or solid nanoparticles [22], limit the range of readily available bubble nuclei: this will result in no cavitation occurring below a certain threshold, and strong cavitation occurring above that threshold, thus skewing the distribution to the right. Secondly, even when cavitation nucleation entirely relies on stochastic processes, this type of chaotic behavior is described by bifurcation diagrams that enable a number of discrete modes of oscillation to co-exist for exactly identical ultrasound and environmental conditions [40]. The consequence of this, when limited to a finite range of achievable excitation pressures, is that the overall distribution of cavitation emissions may be the result of discrete overlapping Gaussians and non-Gaussians corresponding to these discrete modes. Overall, therefore, cavitation emissions in practice are likely to be non-Gaussian due to limitations imposed by the range of available pressures at a particular depth, the pre-defined distribution of cavitation nuclei, and discrete bubble behaviors imposed by bifurcation diagrams associated with the chaotic process. Lastly, the use of band-limited sensor arrays can add amplitude, frequency, and phase variations to the received data that often are not accounted for when the array is poorly calibrated or cannot be accurately calibrated. These aberrations can further cause the broadband bubble emissions to deviate from a Gaussian distribution.

To propel clinical adoption of PAM both for diagnostic and treatment monitoring purposes, new beamforming approaches should be introduced that allow improved source resolvability and robustness to calibration errors. In this paper, a new passive acoustic beamforming algorithm is proposed that uses the mean and variance of the array output, as well as its HOS, in the calculation of the weights, to exploit as much information hidden in the recorded signals as possible. Such a beamforming approach is expected to provide increased interference suppression and subsequent improved source resolvability by decreased dependence on accurate array calibration. The performance of the beamformer is evaluated through simulations and in vitro experimentation to assess improvement of the spatial source resolvability of PAM.

II. THEORY

A. PAM background

A PAM map is a representation of the spatial energy distribution of nonlinear acoustic sources, each of them with specific source strength. Considering a monopole source at a position \mathbf{r} within a region of interest, its acoustic source strength could be estimated by beamforming. The beamforming process involves back-propagating (i.e. time-delaying and amplitude-compensating) the signals p_i , received by each element at location \mathbf{r}_i of an array, to location \mathbf{r} , apodizing them by applying weights w_i , for noise and interference suppression, and coherently summing them.

$$q = \sum_{i=1}^N w_i 4\pi |\mathbf{r}_i - \mathbf{r}| p_i \left(t + \frac{|\mathbf{r}_i - \mathbf{r}|}{c} \right) \quad (1)$$

where c is the speed of sound of the medium, N the number of detectors, t is the time variable, and variables in bold signify vectors. In matrix format, (1) is re-written as:

$$q = 4\pi \mathbf{w}^T \mathbf{D}(\mathbf{r}) \mathbf{p}(\mathbf{r}, t) \quad (2)$$

where $\mathbf{D}(\mathbf{r}) = \text{diag}[|\mathbf{r}_1 - \mathbf{r}|, \dots, |\mathbf{r}_N - \mathbf{r}|]$.

Source energy is then calculated by integrating the square of source strength over a period of time T_p .

$$\Psi(\mathbf{r}) = (4\pi/\rho c) \mathbf{w}^T \mathbf{D}(\mathbf{r}) \mathbf{R}_p(\mathbf{r}) \mathbf{D}(\mathbf{r}) \mathbf{w} \quad (3)$$

where $\mathbf{R}_p(\mathbf{r}) = \int_t^{t+T_p} \mathbf{p}(\mathbf{r}, t) \mathbf{p}(\mathbf{r}, t)^T dt$, and ρ is the density of the medium.

Estimation of source energy is, therefore, dependent on the choice of \mathbf{w} . As already briefly discussed in the introduction, there is a range of beamforming techniques available for PAM, differentiated by the way each of them apodizes the array output. The non-adaptive beamformer (TEA) apodizes equally all the elements of the array, whereas the data-adaptive beamformers, CB and RCB, calculate the weights by solving an optimization problem dependent on the recorded array signals. A summary of the weight calculation for the different beamformers is presented in Table I. It should be noted at this point that weight calculation for RCB is indirect via the optimization of the steering vector, accounting for array calibration and steering vector uncertainty. The minimization problems for CB and RCB rely on the variance of the recorded signals, and the covariance matrix \mathbf{R}_p is used, assuming a Gaussian distribution of the mixture of signals received at the array. An alternative approach is presented in the next section based on HOS of the recorded signals combined with the flexibility of RCB under steering vector uncertainty conditions.

B. Robust Beamforming by Linear Programming (RLPB)

The HOS beamforming technique for PAM used in this

paper is RLPB [40]. Considering an array of N sensors, the vector of the array outputs, steered to a certain location, is:

$$\mathbf{x}(n) = [x_1(n), \dots, x_N(n)]^T \quad (4)$$

The beamformer output for a vector of N weights is

$$\mathbf{y}(n) = \mathbf{w}^T \mathbf{x}(n) \Leftrightarrow \mathbf{Y} = \mathbf{X}^T \mathbf{w} \quad (5)$$

Instead of minimising the variance of the beamformer output, the proposed beamformer minimises the l_∞ -norm of the beamformer output [40]:

$$\min_{\mathbf{w}} \|\mathbf{X}^T \mathbf{w}\|_\infty \quad \text{s.t. } |(\mathbf{a} + \mathbf{e})^T \mathbf{w}|_\infty \geq 1 \text{ for all } \mathbf{e} \in \mathcal{E} \quad (6)$$

where $\mathbf{w}, \mathbf{a}, \mathbf{e} \in \mathbb{R}^M$ and $\mathbf{X} \in \mathbb{R}^{M \times N}$. The steering vector \mathbf{a} , generally defined as a complex vector, describes in array processing terminology the path between the array elements and a source in the far-field. Specifically in the context of PAM, the sources of interest are mainly broadband and located in the near field of the array. Since the inverse distances correspond to the delays that are already applied to the array signals at the initial PAM stage of signal pre-steering and amplitude compensation, the steering vector simplifies to the unity vector. The constraint imposed in the minimisation problem in (6) allows the steering vector \mathbf{a} to vary by a steering vector error \mathbf{e} . This creates an uncertainty region, similar to that of RCB, which accounts for steering vector mismatches in order to ensure that the magnitude response of the beamformer for the signal-of-interest is not attenuated, while interfering signals are suppressed. The uncertainty region is modelled as a rhombus $\mathcal{E} = \{\mathbf{e} | \|\mathbf{e}\|_1 \leq \varepsilon_1\}$, in which ε_1 defines the size of the uncertainty region.

The main limitation in efficiently solving the problem in (6) is the infinite number of constraints, and therefore, the problem is reformulated [40]:

$$\min_{\mathbf{w}} \|\mathbf{X}^T \mathbf{w}\|_\infty \quad \text{s.t. } \mathbf{a}^T \mathbf{w} - \varepsilon_1 \|\mathbf{w}\|_\infty \geq 1 \text{ for all } \mathbf{e} \in \mathcal{E} \quad (7)$$

The new formulation in (7) contains only a single constraint and it can be converted in a linear programming problem using the extra variables $u, z \in \mathbb{R}$:

$$\min_{\mathbf{w}, u, z} u \quad \text{s.t.} \quad \begin{cases} -u \mathbf{1}_N \leq \mathbf{X}^H \mathbf{w} \leq u \mathbf{1}_N \\ \mathbf{a}^T \mathbf{w} \geq 1 + \varepsilon_1 z \\ -z \mathbf{1}_M \leq \mathbf{w} \leq z \mathbf{1}_M \end{cases} \quad (8)$$

In the present work, the linear programming problem is solved using the primal-dual infeasible-interior-point algorithm specifically designed for large-scale linear programming problems [41].

TABLE I
WEIGHT CALCULATION FOR TEA, CB, RCB, AND
RLPB

Method	Weight calculation
TEA	Constant – $\mathbf{w} = (\frac{1}{N})\mathbf{1}$ (9)
CB	$\min_{\mathbf{w}} \mathbf{w}^T \mathbf{D}(\mathbf{r}) \mathbf{R}_p(\mathbf{r}) \mathbf{D}(\mathbf{r}) \mathbf{w}$ s.t. $\mathbf{w}^T \mathbf{a} = 1$ (10)
RCB	$\min_{\mathbf{a}} \mathbf{a}^T \mathbf{D}(\mathbf{r}) \mathbf{R}_p(\mathbf{r}) \mathbf{D}(\mathbf{r}) \mathbf{a}$ (11) s.t. $\ \mathbf{a} - \bar{\mathbf{a}}\ ^2 \leq \varepsilon$
RLPB	$\min_{\mathbf{w}} \ \mathbf{X}^T \mathbf{w}\ _{\infty}$ s.t. $\mathbf{a}^T \mathbf{w} - \varepsilon \ \mathbf{w}\ _{\infty} \geq 1$ (12) $\mathbf{a}, \bar{\mathbf{a}}$ is the actual and nominal steering vector

As it is also the case for RCB, the value of ε_1 , the uncertainty parameter, significantly affects the performance of the beamformer, and the selection of the appropriate value depends on different factors. For any setup configuration, a characterisation of ε_1 needs to be performed to find the best compromise between interference suppression and tolerance in steering vector mismatches. As the value of ε_1 increases, the uncertainty region expands allowing more flexibility to the steering vector and therefore, calibration errors can be addressed more efficiently. However, interfering signals will not be as efficiently suppressed as they would be in the case of a smaller ε_1 , resulting in errors in the source energy estimation and spatial resolution of the beamformer. In [40] a coarse upper limit of ε_1 is defined, $\varepsilon_1 \leq \|\mathbf{a}\|_1$, that ensures the minimisation problem is feasible. It is also suggested that *a priori* information on the causes of steering vector mismatches can be exploited to acquire a more optimal value for ε_1 .

In the context of PAM, RLPB can be combined with (2) and (3) to generate maps of source energy. Attempting to provide a physical meaning of the optimisation used in RLPB, it would be useful to consider, first, the optimisation problem in RCB. Minimisation of the variance of the array output aims at minimising the power of the signals originating from locations other than the location of interest (i.e. interferences), while preserving the power of the desired signals. Considering the problem from a statistical point of view, it is attempted to decrease the variance of the Gaussian distribution of the array output, interpreted as more signal samples approaching the mean (assuming a zero mean). However, when the distribution of the array output deviates from Gaussian, then such an optimisation is expected to not be sufficient for interfering signals suppression. Therefore, minimisation of the variance along with all the other HOS (e.g. skewness, kurtosis etc.) of the recorded signals is proposed with RLPB to address this problem.

As far as the weights calculated via the optimisation problem are concerned, it is important to point out that they are originally defined [40] as complex numbers. For reasons of simplicity and consistency with RCB, in the present work \mathbf{w} is represented as a vector of real positive numbers, thus only allowing adjustments of the amplitude of the individual element signals as part of the beamforming process. Without

loss of generality, \mathbf{w} can be defined as complex to also allow adjustments in phase. Table I summarizes the optimization problem for the weight calculation for TEA, CB, RCB and RLPB.

At this point it is important to point out the different computational complexity of the algorithms in Table I, resulting in highly variable processing times depending on the available hardware and software, and the PAM parameters. In the present work, for a typical map of 660 voxels and signals corresponding to 80μsec of recording, TEA and RCB generate maps at a similar frame rate of 0.25Hz, whereas for RLPB the frame rate is approximately 400 times lower. Such performance is based on the use of built-in MATLAB functions, and involves no optimisation and parallelisation of the process. It is important to note that the similar performance of TEA and RCB is due to the relatively short data set length. Increasing the number of time samples would increase the computation time of RCB nonlinearly, and the difference in frame rate between TEA and RCB is going to be more apparent. Comparing the computational complexity of RCB and RLPB, the most computationally expensive part is eigen-decomposition of the covariance matrix in RCB and solving the linear programming problem in RLPB. Interior-point-method and its variations provide accurate solutions to large-scale linear programming problems, and they can run in polynomial time with respect to the number of input variables [42]. Since it is an iterative algorithm, parallelization is not possible, and the same applies to the eigen-decomposition. However, the use of optimized commercially available

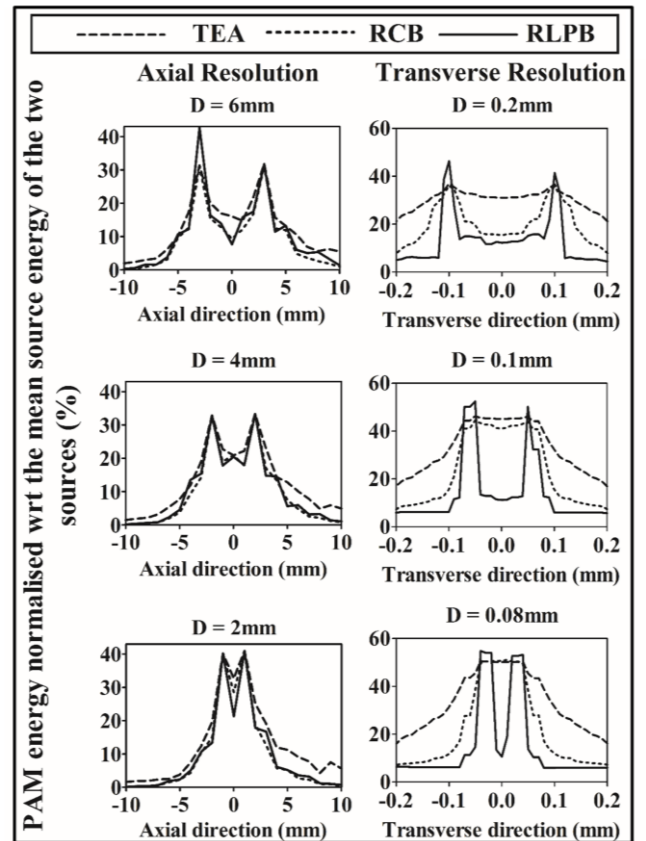


Fig. 1. Simulation results of the transverse and axial resolution of PAM for the three beamforming algorithms (TEA, RCB, RLPB) for a fixed distance between the sources and the array of elements, as the distance between the two single sources decreases with respect to the theoretical value.

software along with parallelization of other components in the PAM process can provide real-time performance in the context of PAM using either of the two beamformers. Additionally, combination of various beamformers for the generation of a single PAM map could provide a good compromise between resolution and real-time PAM map generation.

III. NUMERICAL SIMULATIONS

Initial evaluation of the proposed algorithm is performed using numerical simulations of bubble sources responding to an incident ultrasonic field. The spatial source resolvability of PAM in conjunction with RLPB beamformer is assessed and compared against the performance of TEA and RCB. It is important to note that the results presented in this section aim at providing an initial analytical basis of the benefits of a HOS-based beamformer in terms of single source resolvability. There are several limitations identified in these simulations that are aimed to be addressed with the in vitro experiment presented in Section IV.

The Keller-Miksis model [43]–[45] of large-amplitude radial oscillations from a single gas bubble in an infinite medium of compressible fluid has been chosen to describe the acoustic dynamics of two bubbles in the presence of an incident acoustic field, and consecutively, the pressure waves radiated by the bubbles are calculated [46]. The emissions generated by the two gas bubbles propagate spherically, and they are recorded by a linear array placed at a fixed distance from the bubbles. The array element configuration and bandwidth are chosen to mimic the commercially available L11-4v ultrasound transducer (central frequency 6.25 MHz, 128 elements, pitch 0.298–0.302mm, Verasonics, Inc., Kirkland, WA). White Gaussian noise is added to the acoustic signals at a level consistent with electronic noise recordings from the Verasonics Vantage Research Ultrasound System (Verasonics, Inc., Kirkland, WA), namely approximately 0.07% of the dynamic range of the system. The acoustic emissions are then processed with three beamformers (TEA, RCB, RLPB) independently. Mapping of each source with the three beamformers results in different spatial distribution of the energy. The level and extent of blurring around the location of each bubble resulting from the choice of the beamforming algorithm determines how close two adjacent regions can be

brought but still be resolvable.

The parameters chosen in these simulations for the Keller-Miksis model and the PAM algorithm are summarised in Table II. To avoid constructive and destructive interference of passively received emissions when bubbles respond in phase, the radius of the second bubble is chosen to be slightly different to the first in order to prevent degradation of the PAM spatial resolution. However, the two chosen radii must yield comparable levels of acoustic emissions from both bubbles to avoid shadowing during PAM; therefore, the chosen radii are almost equal. Finally, as far as the data-adaptive beamformers are concerned, the effect of the ε parameter in the PAM spatial resolution is evaluated.

According to the theoretical limits of passive imaging resolution (non-adaptive beamforming) [47] for the linear array presented in Table II, and speed of sound of the medium equal to 1482m/s, the minimum resolvable distance between the two sources is 0.4mm transversely and 6.3mm axially. Therefore, the distances chosen for the assessment of the spatial source resolvability for all beamformers are 0.2mm, 0.1mm, and 0.08mm for the transverse resolution, i.e. along the direction parallel to the array aperture, and 6mm, 4mm, and 2mm for the axial resolution, i.e. orthogonal direction with respect to the array aperture. The transverse and axial PAM energy profiles respectively for all three beamforming techniques at each distance between the two sources mentioned above are presented in Fig.1. Resolvability of the two sources, which in this case is equivalent to interference suppression capability in the region between the two sources, is quantified using Rayleigh's criterion for the diffraction limit to resolution [48]. This criterion specifies the minimum separation angle between two light sources in order to be resolved as two distinct objects [49] and in practice it requires the trough between the two sources to be at least 26.3% of the peak. The parameter epsilon for these simulations has been chosen to be equal to 5, the lower value among those reported in Table II, to provide improved interference suppression considering that the array calibration is known. It should be noted that this value of epsilon is not necessarily the optimal choice for all distances in Fig.1, and further optimization should be performed to determine it with respect to source resolvability.

For a source separation distance larger than 2mm in the axial direction, all three beamformers perform equally well with only marginal improvements provided by the more advanced beamformers. However, at the smallest axial distance (2mm) considered, TEA fails to meet the criterion for source separation, and the trough provided by RCB (28%) is almost equal to the threshold dictated by Rayleigh's criterion. On the other hand, RLPB performs significantly better providing a trough of approximately 47%.

In the transverse direction, at a distance of 0.2mm between the two sources TEA clearly struggles to distinguish the two sources, whereas the two more advanced beamformers perform significantly better, providing troughs higher than the required resolvability threshold. As distance decreases, namely 0.1mm, RCB also fails to resolve the two sources providing a trough of 6.5%, whereas for RLPB is

TABLE II
NUMERICAL SIMULATIONS PARAMETERS

	Parameter	Value
Keller-Miksis model	Bubble 1 radius (R_0)	3 μ m
	Bubble 2 radius (R_1)	2.9 μ m
	Fundamental frequency	0.5MHz
	Driving pressure	1MPa
	Number of cycles	20
	Distance between bubbles and array	75mm
PAM	Sampling Frequency (F_s)	25MHz
	Speed of sound (c)	1482m/s
	Number of linear array elements	128
	Linear array bandwidth	4–11MHz
	Parameter ε values	5, 10, 15, 20
L11-4v array	Bandwidth	4–11MHz
	Central frequency	6.25MHz
	Number of sensors	128
	Pitch	0.298–0.302mm

significantly higher than the threshold, and it is the only beamformer that enables a clear distinction between the two sources 0.08mm apart.

As far as the effect of the ε parameter is concerned, there is a need for compromise between array steering vector mismatch correction and interference suppression capability. Since in these simulations the array element positions are perfectly known, the performance of the two optimal beamformers should improve as the value of ε decreases, achieving higher levels of interference suppression. To investigate the effect of ε under these simulated conditions, the level of the trough between the two sources in the PAM energy profiles of RCB and RLPB for different values of ε , namely $\varepsilon = 5, 10, 15$, and 20 , at different distances D between the two sources has been calculated and presented in Fig. 2.

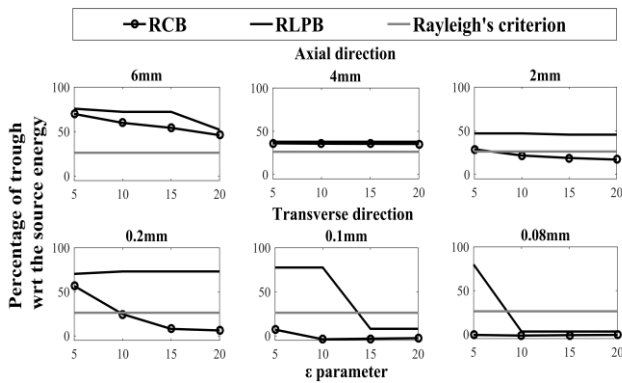


Fig. 2. Simulation results on the effect of parameter ε , which varies between 5 and 20 on the axial and transverse PAM resolvability in the case of two single sources separated by different distances, placed at 75mm away from a linear array.

In the axial direction, at 6mm and 4mm between the two sources, both RCB and RLPB can distinguish the two sources regardless of the value of ε . However, when sources are 2mm apart, RCB is only marginally able to resolve the two sources and only for small values of ε , namely ε equals 5. On the other hand, RLPB demonstrates a much more stable behaviour, consistently resolving the two sources in the range of ε attempted in these simulations without a considerable drop in the level of the trough as ε increases. Therefore, it is considered more robust in terms of interference suppression ability, at distances larger than its resolvability limit.

As far as the transverse resolution is concerned, similar conclusions can be drawn. For a distance of 0.2mm between the two sources RLPB is able to distinguish the two sources for the whole range of ε used in these simulations, and its performance does not degrade substantially as ε increases, proving once again its robustness in terms of interference suppression capability against the chosen value of ε . On the other hand, RCB is only able to distinguish the two sources for ε being equal or smaller than 10. Additionally, the decrease in the trough as ε increases is dramatic, namely 87% as ε goes from 5 to 20. At the transverse resolvability limit for RLPB (0.08mm), it has been observed that RLPB can only resolve the two sources for small values of ε , i.e. ε equal to 5, and then its performance degrades significantly as ε increases. Such behaviour on the resolvability limit is common between the two beamformers with the only

difference being that for small ε values, that allow resolvability, the trough level is much higher for RLPB (80% at 0.08mm for $\varepsilon=5$) compared to RCB (56.7% at 0.2mm for $\varepsilon=5$) providing cleared distinction.

IV. EXPERIMENTAL METHODS

A. Experimental rationale

The results of numerical simulations suggest that by taking into account the HOS of the recorded signals, source resolvability and robustness of PAM with respect to interfering signals is improved. However, there are several important aspects of spatio-temporal monitoring of acoustic emissions during ultrasound therapies that have not been incorporated in the simulations. First, the interaction occurring between the emissions of the two acoustic sources due to multi-path propagation, especially when the sources are aligned in the axial direction with respect to the array, is expected to alter the profile of the emissions as these propagate towards the array. Additionally, resolvability of two regions of acoustic activity (e.g. two bubble clouds), instead of two single sources could also be of interest, and potentially more common in clinical practice. At this point it is important to clarify that the origin of the acoustic sources, i.e. heterogeneous nucleation from the medium or pre-seeded artificial nuclei, is not important for the assessment of PAM resolvability, as it is the type of cavitation occurring, and specifically inertial cavitation. Finally, the presence of interfaces and medium variability is expected to impose another challenge on PAM.

To investigate the performance of the two adaptive beamforming algorithms, RCB and RLPB, under such a challenging situation, and provide additional insight on the PAM spatial source resolvability, the in vitro experiment presented in Fig.3 has been designed and implemented.

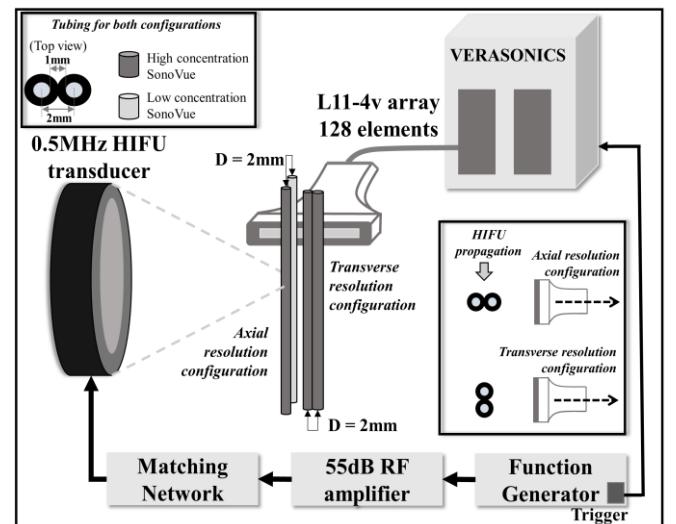


Fig. 3. Experimental setup involving two pieces of PVC tubing with SonoVue of different concentrations in flow, placed at the focus of a HIFU transducer driven at 0.5MHz. The HIFU transducer is co-aligned with a 4–11 MHz linear array of 128 elements for passive recording of acoustic emissions. These emissions are processed using PAM combined with each of the two beamforming algorithms (RCB, RLPB) to provide maps of sources of acoustic emissions. The two PVC tubing pieces are placed either on the axial or the transverse direction with respect to the linear array, to assess the transverse and axial PAM resolution respectively.

B. Experimental apparatus

A 0.5MHz spherically focused, single-element ultrasound transducer (H107 SN27; Sonic Concepts, Bothell, WA) with active diameter 64mm, focal length 62.4mm, and a central rectangular cut-out of dimensions 13x45mm² is placed in a large tank filled with degassed, filtered water. The transducer is connected through a matching network to a function generator (33250A, Agilent Technologies, Santa Clara, CA), and it is driven on burst mode (2000-cycles sinusoid signal of burst period 200ms), at its fundamental frequency at 1.3MPa (free field peak rarefactional pressure), after amplification by a 55dB power amplifier (E&I A300; Rochester NY).

An L11-4v linear array transducer (Verasonics, Inc., Kirkland, WA) with characteristics presented in Table II is placed perpendicular to the HIFU transducer and co-aligned with the focus of the HIFU transducer. The multi-element array transducer is connected to the Verasonics Vantage Research Ultrasound System (Verasonics, Inc., Kirkland, WA) that allows passive simultaneous recording of the acoustic signals from all elements on the array, and subsequent processing for generation of PAM maps.

Two sections of PVC tubing (Thermo Fisher ScientificTM) of inner diameter 1mm and outer diameter 2mm are placed on a holder, and positioned at the focus of the HIFU transducer. Two configurations are used regarding the position of the tubes with respect to the HIFU transducer and the linear array in order to test PAM resolvability in both axial and transverse direction with respect to the array. The distance between the centres of the tubes is 2mm. By using a separate syringe pump for each tube, SonoVue microbubbles (SV; Bracco Spa, Milan, ITA) flow through the tubes at a constant rate, acting as cavitation nuclei. Parameters for each type of resolvability experiment are listed in Table III.

C. Experimental Procedures

Recording of the acoustic emissions is synchronized with the HIFU exposure by triggering the Verasonics Vantage system, and the receive sampling frequency was four times the central frequency of the linear array (6.25MHz), i.e. 25MHz. At a frame rate of 1Hz, the RF signals are transferred to the memory of the computer and processed using a real-time implementation of RCB-PAM based on a combination of GPU and CPU programming to provide a real-time PAM map and guide the experiment.

PAM resolution is theoretically dictated by the diffraction limits of the passive array given its geometry and bandwidth [47]. Considering the central frequency and aperture of the linear array (Table II), the distance between the sources and the array determines resolvability. Changes in PAM resolution limits due to the application of different beamforming techniques could be assessed either by keeping the array-to-source distance fixed and altering the source separation, or keeping the source separation fixed and altering the array-to-source distance. The second approach has been used here as it is considerably more practical to implement experimentally, although the right-angle setup (HIFU transducer perpendicular to the linear array) is not clinically applicable, but sufficient for comparison between beamformers.

Following alignment of all the components in the setup, the array was initially moved as close as needed to the two

pieces of tubing to enable clear separation of the two sources using the real-time implementation of RCB. This process was repeated both for axial and transverse source separation arrangements, yielding a different initial distance for each configuration.

Adjustments to the concentration of SonoVue flowing through each of the tubes and to the flow rate in each tube were required for both axial and transverse resolution setup configurations. In the case of the axial resolution experiments, the emissions from the tube positioned further away with respect to the linear array were highly attenuated as they propagated through the multiple tubing interfaces. Therefore, a higher concentration of SonoVue (Table III)

TABLE III
IN VITRO SONOVUE DILUTION & FLOW RATE

Parameter	Experiment	Channel	Value
SonoVue Dilution	Axial Resolution	Front*	2ml/L
		Back*	40ml/L
	Transverse Resolution	Front**	40ml/L
		Back**	40ml/L
Flow rate	Axial Resolution	Front*	0.4ml/min
		Back*	0.2ml/min
	Transverse Resolution	Front**	0.3ml/min
		Back**	0.4ml/min

* with respect to the array of detectors

** with respect to the HIFU transducer

was flowed through the distal tube compared to the proximal tube, in order to ensure comparable levels of acoustic emissions due to inertial cavitation being recorded by the elements of the array. Additionally, PAM amplitude has been used to dynamically control the flow rate in each tube and ensure comparable level of received acoustic emissions from both tubes. A similar optimization procedure was followed when the tubes were placed along the transverse axis with respect to the array. Since the acoustic emissions originating from each tube propagate through the same layers of tubing towards the array, no adjustment in the concentration of SonoVue in each tube was necessary. However, the position of each of the tubes with respect to the focal region of the HIFU transducer might cause a small difference in focal pressure applied in each of the tubes, and, therefore, PAM amplitude was used as feedback to dynamically control the flow rate.

Starting from the initial position, the array was gradually moved further away using an automated positioning system, and data was recorded continuously. Post-processing of the recorded raw time domain signals involves the generation of PAM maps for each set of data using either RCB or RLPB. Prior to beamforming, the recorded signals are time-windowed, corresponding to 80μs time of recording at the beginning of the exposure, and then filtered using a custom high-pass filter implemented in MATLAB with a cut-off frequency at 1.2MHz to eliminate the first two harmonics observed in the spectrum of the recorded signal. Therefore, the remaining signal consists only of broadband noise due to inertial cavitation, which is fed in the PAM algorithm.

Although the ε parameter is expected to affect the performance of both optimal beamforming algorithms, it is not in the scope of the present in vitro experiment to investigate it with respect to the two beamforming approaches. Instead, ε was set to 10 throughout the

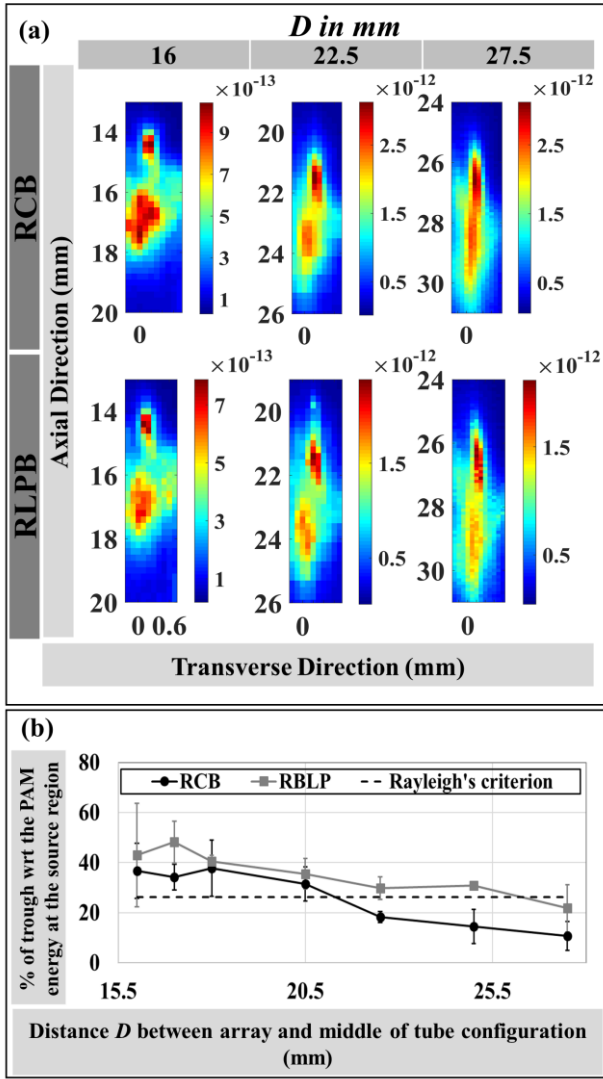


Fig. 4. (a) PAM corresponding to RCB and RLPB, for different distances between the two PVC tubing pieces and the linear array, varying between 16mm and 27.5mm. The tubing parts are placed along the axis of the array (shown by black line) to assess the axial resolution of PAM. (b) PAM source region resolvability analysis in the transverse direction based on Rayleigh's criterion that requires the level of the trough between the two regions to exceed 26.3% of the level of the source region energy. The trough is calculated in each case based on the peak intensity projection line profile of each map, with respect to the source region with the lowest PAM energy. The mean and standard deviation of the trough is plotted with respect to the distance between the array and the middle of the tubing configuration. The threshold for the two source regions to be resolvable is displayed with a black dashed line (- -), and results above this line indicate successful resolvability.

experiment for both beamformers ensuring correct source localization and estimation of the size of the cavitation regions at the initial point of the experiment, i.e. smallest distance between the sources and the array.

V. EXPERIMENTAL RESULTS

A. Axial resolution

Fig.4a shows characteristic PAM maps generated using RCB and RLPB for two cavitating regions, bound by the two pieces of tubing, positioned axially at different distances D from the array and at a fixed separation from each other. The distance D , ranging between 16mm and 27.5mm, is defined as the distance between the middle point of the two

maximum PAM energies calculated for the two cavitating regions and the middle element of the array. This is an approximate calculation since we are primarily interested in the comparison of the spatial resolution provided by the two methods, and not an accurate definition of the resolvability limits of the two beamforming techniques, which is expected to be highly dependent on the experimental conditions. The color axis of each map is independent and corresponds to the dynamic range observed in the specific map.

To quantify resolvability of the two regions of cavitation activity, Rayleigh's criterion is used, as described in section III. In this case, since the energy in the two regions is not always equal, this criterion is defined with respect to the region that demonstrates the lowest PAM energy. Peak intensity projection is performed for each map along the transverse direction, and a line profile of peak intensity with respect to the axial axis is generated. Calculation of the trough for each PAM map in Fig.4a for both beamforming algorithms is performed on these line profiles, and the results are presented in Fig.4b.

Analysis of the axial line profiles on the PAM maps provides an approximation of the resolution limits achieved by the beamforming algorithms. It is observed that for RCB, Rayleigh's criterion for resolvability is no longer satisfied at $D = 22.5$ mm. The limiting value of D is much higher in the case of RLPB (27.5mm), constituting an increase in PAM axial resolution of approximately 22%.

By observing the color maps for each distance in Fig.4a, it is concluded that the maximum source energy estimated through each optimization process is comparable. The maximum source energy estimated by RLPB is between 70% and 85% of the corresponding energy estimated by RCB for all pairs of maps. It should be noted at this point that the source energy on the PAM maps is expressed in arbitrary units, with the same scale used across all maps presented in the paper. These arbitrary units could be transformed into Joules, if an array calibration were performed as described in [50]. However, either in arbitrary units or in Joules, source energy estimates highly depend on the optimization performed by each beamformer, and thus, by the choice of epsilon. This could justify the observed difference in source power estimates between RCB and RBLP, and therefore, PAM energy levels should not be directly compared across beamformers. The key difference between the two beamforming algorithms is the ability to suppress the interference between the two source regions. Although the diameter of each cavitation region is limited to

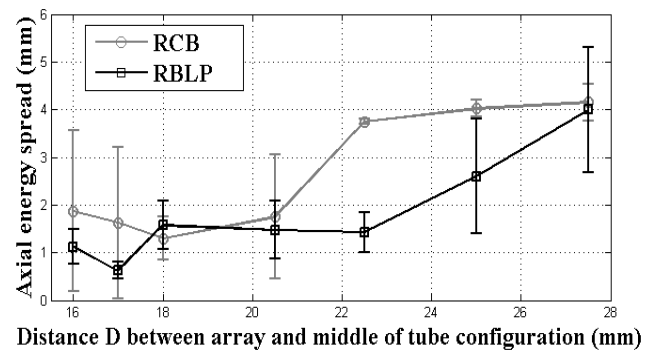


Fig. 5. Axial energy spread analysis for RCB and RLPB with respect to distance D between the array and the middle of tube configuration.

1mm, due to the physical size of the channel, in RCB this size seems to be exceeded compared to RLPB. This results in overlap of the two source regions and limits resolvability. The combination of the point spread function resulting from the weights derived by each beamforming algorithm, and the ability of each beamformer to deal with multi-source interference [27] is potentially the reason behind the different elongation observed between the two beamforming algorithms.

To further support the above observation, axial energy spread analysis is performed based on the peak intensity profile of each map (Fig.5). The energy spread is calculated for the lowest energy source region (if the two are distinguishable), at 73.7% of its peak energy, which corresponds to the threshold for source resolvability employed previously. Considering the dimensions and arrangement of tubing (Fig.3), the maximum energy spread for one source region should be close to 2mm, taking into account small errors in tube alignment, and differences in source strength resulting in different energy spread. In Fig.5 it is observed that RLPB energy spread is consistently lower than that of RCB for the majority of the distances presented, allowing improved source resolvability due to better interference suppression. At the source resolvability threshold of RCB, namely 22.5mm, the energy spread doubles, signifying the merging of the two source locations into one, and the same observation is also made for RLPB.

B. Transverse resolution

The same approach is applied to the analysis of the results in the context of transverse positioning of the sources with respect to the array (Fig.6a). Peak intensity projection along the axial direction is now performed to generate line profiles of intensity with respect to the transverse axis. The percent decrease between source energy and off-target energy is subsequently calculated, and the results are presented in Fig.6b.

On an observation basis (Fig.6a) RCB can visually separate the two cavitation regions at 230mm, whereas RLPB is still capable of distinguishing the two regions even at 300mm from the array. After applying Rayleigh's criterion for resolvability (Fig.6b), the above limits become stricter. RCB fails to satisfy the resolution criterion at all distances presented in the figure, whereas for RLPB the distance at which the criterion is no longer satisfied is 260mm.

Another important observation from Fig.6a is the increase of the size of the cavitation region in the axial direction as the distance from the array increases, and the difference in this elongation between RCB and RLPB. As already discussed, the difference in the elongation of the cavitation region is the reason for the decreased resolvability in the axial direction of RCB compared to RLPB. The results shown in Fig.6a enhance this conclusion, demonstrating the elongation of each source region even in the absence of another cavitating region in front or behind it.

The elongation in the axial direction due to the large distance between the tubes and the array does not allow correct localization of the tubes. The distance D is verified in this case by the arrival time, based on the speed of sound in water, on the array elements of the reflection of the incident wave (at the driving frequency) from the proximal to the HIFU transducer tube wall. At this point it would be interesting to point out that the location of the maximum on

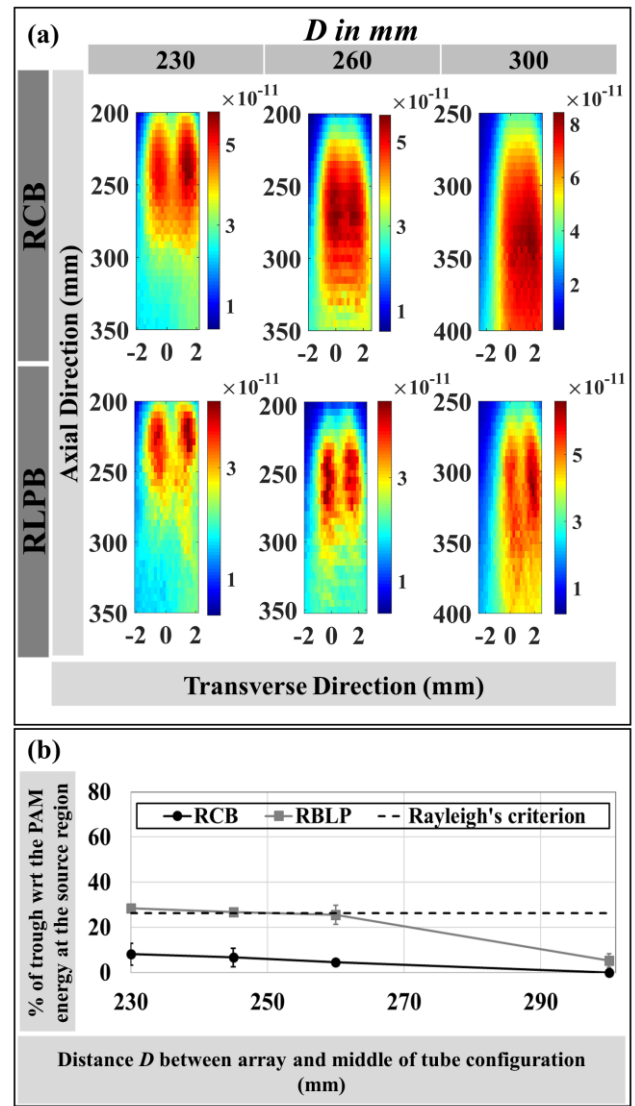


Fig. 6. (a) PAM corresponding to RCB and RLPB, for different distances between the two PVC tubing pieces and the linear array, varying between 230mm and 300mm. The tubing parts are placed along the transverse direction of the array to assess the transverse resolution of PAM. (b) PAM source region resolvability analysis in the transverse direction based on Rayleigh's criterion that requires the level of the trough between the two regions to exceed 26.3% of the level of the source region energy. The trough is calculated in each case based on the peak intensity projection line profile of each map, with respect to the source region with the lowest PAM energy. The mean and standard deviation of the trough is plotted with respect to the distance between the array and the middle of the tubing configuration. The threshold for the two source regions to be resolvable is displayed with a black dashed line (- -), and results above this line indicate successful resolvability.

the RLPB PAM maps is closer to the true tube location compared to RCB.

Analysis of the line profiles on the PAM maps (Fig.6b) provides an approximation of the resolution limits for the two beamforming algorithms. For RCB, Rayleigh's criterion for resolvability is no longer satisfied at a sources-to-array distance of 230mm. On the other hand, this limit is much higher in the case of RLPB, namely 260mm, constituting an increase in PAM axial source resolvability of 13%.

Considering the worst-case scenario of sources cavitating adjacent to the two proximal tubing walls, (source-to-source distance of 1mm), the maximum theoretical distance from the array for the regions to be resolvable is approximately 30mm axially and 180mm transversely. Therefore, the axial resolution of RLPB approaches the theoretical resolution

limit dictated by diffraction, whereas the theoretical transverse resolution limit has been surpassed by both beamforming algorithms.

VI. CONCLUSION

A novel optimal passive array beamforming algorithm has been proposed in this paper that exploits the HOS of the received acoustic signals to improve the spatial resolution of PAM. By minimizing the l_∞ -norm of the array output, RLPB exploits the higher order moments of the array signals. Simulations and in vitro experimentation demonstrated the ability of RLPB to outperform all other currently available beamforming algorithms in terms of source resolvability, for a significant but addressable change in processing time.

According to numerical simulations, RLPB provides significantly improved transverse and axial resolution relative to either TEA or RCB. Transversely, the RLPB is capable of resolving sources that are separated by less than half the distance of those resolvable by RCB. Axially, RLPB is still able to distinguish sources separated by 2 mm which are unresolvable by RCB.

An additional advantage of the RLPB algorithm is its robustness to variations in the optimization parameter ϵ with respect to interference suppression capability. High levels of interference suppression are maintained for larger regions of uncertainty, allowing subsequently more robust handling of calibration errors compared to RCB. This feature is expected to significantly enhance the performance of PAM for in vivo applications where array calibration cannot always be accurate, and interferences from nearby source regions, need to be eliminated for accurate source energy estimation.

In vitro experimentation verified the relative spatial resolutions achieved by RCB and RLPB, under more clinically relevant conditions with multiple sources of cavitation present, and regions of cavitation to be resolved. Results demonstrated improved performance of RLPB compared to RCB, providing 22% and 13% enhancement in the axial and transverse PAM resolution respectively. The resolution improvement is believed to originate from the combination of narrower point spread function for a single source, as the simulations suggest, with better suppression of interfering signals from multiple sources.

Application of the proposed method in vivo is expected to provide improved source resolvability and facilitate spatial correlation between acoustic activity and anticipated bioeffects. A significant factor that needs to be taken into consideration in the transition from in vitro to in vivo application of RLPB-PAM is the presence of multiple tissue layers in the acoustic propagation path. This would result in phase changes in the propagating signals that could be addressed by considering the weights in RLPB as complex numbers. Such a modification is expected to further improve performance, but also increase the computational complexity of the beamforming algorithm.

In conclusion, it is anticipated that the proposed beamforming algorithm will significantly improve PAM source resolvability, allowing statistical information in the HOS of the acoustic signals to be exploited. The demonstrated resolvability enhancement due to improved interference suppression, and its robustness in changes of

the size of the uncertainty region, allowing subsequently improved mitigation of calibration errors, brings PAM a step closer to its clinical adoption. In clinical ultrasound applications where the targeted region is deeper inside the body, e.g. the spine, or when regions of acoustic activity to be resolved are very close to each other, as is the case in drug delivery, RLPB could provide the source resolvability required to ensure both safety and efficacy of the treatment. Finally, combination of the proposed beamformer with super-resolution techniques could enable enhanced acoustic source localization that can propel not only the therapeutic but also the diagnostic applications of PAM.

REFERENCES

- [1] J. E. Kennedy, "High-intensity focused ultrasound in the treatment of solid tumours," *Nat. Rev. Cancer*, vol. 5, no. 4, pp. 321–327, Apr. 2005.
- [2] C. M. C. Tempany, E. A. Stewart, N. McDannold, B. J. Quade, F. A. Jolesz, and K. Hynynen, "MR Imaging-guided Focused Ultrasound Surgery of Uterine Leiomyomas: A Feasibility Study," *Radiology*, vol. 226, no. 3, pp. 897–905, Mar. 2003.
- [3] E. A. Stewart, W. M. W. Gedroyc, C. M. C. Tempany, B. J. Quade, Y. Inbar, T. Ehrenstein, A. Shushan, J. T. Hindley, R. D. Goldin, M. David, M. Sklair, and J. Rabinovici, "Focused ultrasound treatment of uterine fibroid tumors: Safety and feasibility of a noninvasive thermoablative technique," *Am. J. Obstet. Gynecol.*, vol. 189, no. 1, pp. 48–54, Jul. 2003.
- [4] E. A. Stewart, J. Rabinovici, C. M. C. Tempany, Y. Inbar, L. Regan, B. Gastout, G. Hesley, H. S. Kim, S. Hengst, and W. M. Gedroyc, "Clinical outcomes of focused ultrasound surgery for the treatment of uterine fibroids," *Fertil. Steril.*, vol. 85, no. 1, pp. 22–29, Jan. 2006.
- [5] W. Sass, M. Bräunlich, H. P. Dreyer, E. Matura, W. Folberth, H. G. Preismeyer, and J. Seifert, "The mechanisms of stone disintegration by shock waves," *Ultrasound Med. Biol.*, vol. 17, no. 3, pp. 239–243, 1991.
- [6] R. Carlisle, J. Choi, M. Bazan-Peregrino, R. Laga, V. Subr, L. Kostka, K. Ulbrich, C.-C. Coussios, and L. W. Seymour, "Enhanced tumor uptake and penetration of virotherapy using polymer stealthing and focused ultrasound," *J. Natl. Cancer Inst.*, vol. 105, no. 22, pp. 1701–1710, Nov. 2013.
- [7] S. Chen, J. Ding, R. Bekeredjian, B. Yang, R. V. Shohet, S. A. Johnston, H. E. Hohmeier, C. B. Newgard, and P. A. Grayburn, "Efficient gene delivery to pancreatic islets with ultrasonic microbubble destruction technology," *Proc. Natl. Acad. Sci.*, vol. 103, no. 22, pp. 8469–8474, May 2006.
- [8] P. C. Lyon, L. F. Griffiths, J. Lee, D. Chung, R. Carlisle, F. Wu, M. R. Middleton, F. V. Gleeson, and C. C. Coussios, "Clinical trial protocol for TARDOS: a phase I study to investigate the feasibility of targeted release of lyso-thermosensitive liposomal doxorubicin (ThermoDox®) using focused ultrasound in patients with liver tumours," *J. Ther. Ultrasound*, vol. 5, Nov. 2017.
- [9] A. V. Alexandrov, A. M. Demchuk, W. S. Burgin, D. J. Robinson, and J. C. Grotta, "Ultrasound-Enhanced Thrombolysis for Acute Ischemic Stroke: Phase I. Findings of the CLOTBUST Trial," *J. Neuroimaging*, vol. 14, no. 2, pp. 113–117, Apr. 2004.
- [10] N. Lipsman, M. L. Schwartz, Y. Huang, L. Lee, T. Sankar, M. Chapman, K. Hynynen, and A. M. Lozano, "MR-guided focused ultrasound thalamotomy for essential tremor: a proof-of-concept study," *Lancet Neurol.*, vol. 12, no. 5, pp. 462–468, May 2013.
- [11] M. Kinoshita, N. McDannold, F. A. Jolesz, and K. Hynynen, "Targeted delivery of antibodies through the blood-brain barrier by MRI-guided focused ultrasound," *Biochem. Biophys. Res. Commun.*, vol. 340, no. 4, pp. 1085–1090, Feb. 2006.
- [12] N. McDannold, C. D. Arvanitis, N. Vykhodtseva, and M. S. Livingstone, "Temporary Disruption of the Blood-Brain Barrier by Use of Ultrasound and Microbubbles: Safety and Efficacy Evaluation in Rhesus Macaques," *Cancer Res.*, vol. 72, no. 14, pp. 3652–3663, Jul. 2012.
- [13] C. R. Jensen, R. W. Ritchie, M. Gyöngy, J. R. T. Collin, T. Leslie, and C.-C. Coussios, "Spatiotemporal monitoring of high-intensity focused ultrasound therapy with passive acoustic mapping," *Radiology*, vol. 262, no. 1, pp. 252–261, Jan. 2012.
- [14] Y.-F. Zhou, "High intensity focused ultrasound in clinical tumor ablation," *World J. Clin. Oncol.*, vol. 2, no. 1, pp. 8–27, Jan. 2011.

- [15] M. Gyongy, M. Arora, J. A. Noble, and C.-C. Coussios, "Use of passive arrays for characterization and mapping of cavitation activity during HIFU exposure," presented at the IEEE Ultrasonics Symposium, 2008. IUS 2008, 2008, pp. 871–874.
- [16] V. A. Salgaonkar, S. Datta, C. K. Holland, and T. D. Mast, "Passive cavitation imaging with ultrasound arrays," *J. Acoust. Soc. Am.*, vol. 126, no. 6, pp. 3071–3083, Dec. 2009.
- [17] M. Gyongy and C.-C. Coussios, "Passive Spatial Mapping of Inertial Cavitation During HIFU Exposure," *IEEE Trans. Biomed. Eng.*, vol. 57, no. 1, pp. 48–56, Jan. 2010.
- [18] C. R. Jensen, R. O. Cleveland, and C. C. Coussios, "Real-time temperature estimation and monitoring of HIFU ablation through a combined modeling and passive acoustic mapping approach," *Phys. Med. Biol.*, vol. 58, no. 17, p. 5833, Sep. 2013.
- [19] C. D. Arvanitis, M. S. Livingstone, and N. McDannold, "Combined Ultrasound and MR Imaging to Guide Focused Ultrasound Therapies in the Brain," *Phys. Med. Biol.*, vol. 58, no. 14, pp. 4749–4761, Jul. 2013.
- [20] J. Gateau, J. F. Aubry, M. Pernot, M. Fink, and M. Tanter, "Combined passive detection and ultrafast active imaging of cavitation events induced by short pulses of high-intensity ultrasound," *IEEE Trans. Ultrason. Ferroelectr. Freq. Control*, vol. 58, no. 3, pp. 517–532, Mar. 2011.
- [21] J. J. Choi, R. C. Carlisle, C. Coviello, L. Seymour, and C.-C. Coussios, "Non-invasive and real-time passive acoustic mapping of ultrasound-mediated drug delivery," *Phys. Med. Biol.*, vol. 59, no. 17, p. 4861, 2014.
- [22] J. J. Kwan, R. Myers, C. M. Coviello, S. M. Graham, A. R. Shah, E. Stride, R. C. Carlisle, and C. C. Coussios, "Ultrasound-Propelled Nanocaps for Drug Delivery," *Small*, vol. 11, no. 39, pp. 5305–5314, Oct. 2015.
- [23] K. B. Bader, K. J. Haworth, H. Shekhar, A. D. Maxwell, T. Peng, D. D. McPherson, and C. K. Holland, "Efficacy of histotripsy combined with rt-PA in vitro," *Phys. Med. Biol.*, vol. 61, no. 14, p. 5253, 2016.
- [24] R. M. Jones, M. A. O'Reilly, and K. Hynynen, "Transcranial passive acoustic mapping with hemispherical sparse arrays using CT-based skull-specific aberration corrections: a simulation study," *Phys. Med. Biol.*, vol. 58, no. 14, p. 4981, Jul. 2013.
- [25] K. B. Bader, K. J. Haworth, A. D. Maxwell, and C. K. Holland, "Post Hoc Analysis of Passive Cavitation Imaging for Classification of Histotripsy-Induced Liquefaction in Vitro," *IEEE Trans. Med. Imaging*, vol. 37, no. 1, pp. 106–115, Jan. 2018.
- [26] M. A. O'Reilly and K. Hynynen, "A super-resolution ultrasound method for brain vascular mapping," *Med. Phys.*, vol. 40, no. 11, p. 110701, Nov. 2013.
- [27] C. Coviello, R. Kozick, J. Choi, M. Gyöngy, C. Jensen, P. P. Smith, and C.-C. Coussios, "Passive acoustic mapping utilizing optimal beamforming in ultrasound therapy monitoring," *J. Acoust. Soc. Am.*, vol. 137, no. 5, pp. 2573–2585, May 2015.
- [28] K. J. Haworth, T. D. Mast, K. Radhakrishnan, M. T. Burgess, J. A. Kopechek, S.-L. Huang, D. D. McPherson, and C. K. Holland, "Passive imaging with pulsed ultrasound insonations," *J. Acoust. Soc. Am.*, vol. 132, no. 1, pp. 544–553, Jul. 2012.
- [29] S. Lu, H. Hu, X. Yu, J. Long, B. Jing, Y. Zong, and M. Wan, "Passive acoustic mapping of cavitation using eigenspace-based robust Capon beamformer in ultrasound therapy," *Ultrason. Sonochem.*, vol. 41, no. Supplement C, pp. 670–679, Mar. 2018.
- [30] C. Bai, S. Xu, J. Duan, B. Jing, M. Yang, and M. Wan, "Pulse-Inversion Subharmonic Ultrafast Active Cavitation Imaging in Tissue Using Fast Eigenspace-Based Adaptive Beamforming and Cavitation Deconvolution," *IEEE Trans. Ultrason. Ferroelectr. Freq. Control*, vol. 64, no. 8, pp. 1175–1193, Aug. 2017.
- [31] S. J. Norton and I. J. Won, "Time exposure acoustics," *IEEE Trans. Geosci. Remote Sens.*, vol. 38, no. 3, pp. 1337–1343, May 2000.
- [32] J. Capon, "High-resolution frequency-wavenumber spectrum analysis," *Proc. IEEE*, vol. 57, no. 8, pp. 1408–1418, Aug. 1969.
- [33] J. Li, P. Stoica, and Z. Wang, "On robust Capon beamforming and diagonal loading," *IEEE Trans. Signal Process.*, vol. 51, no. 7, pp. 1702–1715, Jul. 2003.
- [34] P. Stoica, Z. Wang, and J. Li, "Robust Capon beamforming," *IEEE Signal Process. Lett.*, vol. 10, no. 6, pp. 172–175, Jun. 2003.
- [35] K. C. Chua, V. Chandran, U. R. Acharya, and C. M. Lim, "Application of higher order statistics/spectra in biomedical signals—a review," *Med. Eng. Phys.*, vol. 32, no. 7, pp. 679–689, Sep. 2010.
- [36] K. Kumatani, J. McDonough, B. Rauch, P. N. Garner, W. Li, and J. Dines, "Maximum Kurtosis Beamforming with the Generalized Sidelobe Canceller," *ResearchGate*, Apr. 2013.
- [37] K. Kumatani, B. Rauch, J. McDonough, and D. Klakow, "Maximum negentropy beamforming using complex generalized Gaussian distribution model," in *2010 Conference Record of the Forty Fourth Asilomar Conference on Signals, Systems and Computers*, 2010, pp. 1420–1424.
- [38] S. Shamsunder and G. B. Giannakis, "Wideband source modeling and localization: a HOS-based approach," in *1991 Conference Record of the Twenty-Fifth Asilomar Conference on Signals, Systems and Computers*, 1991, 1991, pp. 383–387 vol.1.
- [39] H. R. Mohseni, M. L. Kringelbach, M. W. Woolrich, A. Baker, T. Z. Aziz, and P. Probert-Smith, "Non-Gaussian probabilistic MEG source localisation based on kernel density estimation," *Neuroimage*, vol. 87, pp. 444–464, Feb. 2014.
- [40] X. Jiang, W. J. Zeng, A. Yasotharan, H. C. So, and T. Kirubarajan, "Robust Beamforming by Linear Programming," *IEEE Trans. Signal Process.*, vol. 62, no. 7, pp. 1834–1849, Apr. 2014.
- [41] Y. Zhang, "Solving large-scale linear programs by interior-point methods under the Matlab Environment: Optimization Methods and Software: Vol 10, No 1," Department of Mathematics and Statistics, University of Maryland, Baltimore County, Baltimore, MD, TR96-01, Jul. 1995.
- [42] N. Karmarkar, "A New Polynomial-time Algorithm for Linear Programming," in *Proceedings of the Sixteenth Annual ACM Symposium on Theory of Computing*, New York, NY, USA, 1984, pp. 302–311.
- [43] J. B. Keller and M. Miksis, "Bubble oscillations of large amplitude," *J. Acoust. Soc. Am.*, vol. 68, no. 2, pp. 628–633, Aug. 1980.
- [44] J. R. T. Collin and C. C. Coussios, "Quantitative observations of cavitation activity in a viscoelastic medium," *J. Acoust. Soc. Am.*, vol. 130, no. 5, pp. 3289–3296, Nov. 2011.
- [45] I. R. Webb, S. J. Payne, and C.-C. Coussios, "The effect of temperature and viscoelasticity on cavitation dynamics during ultrasonic ablation," *J. Acoust. Soc. Am.*, vol. 130, no. 5, pp. 3458–3466, Nov. 2011.
- [46] S. Yoshizawa, K. Sugiyama, and Y. Matsumoto, "Acoustic Emission from Micro Bubbles in Ultrasound Field," presented at the CAV 2001: Fourth International Symposium on Cavitation, California Institute of Technology, Pasadena, CA USA, 01-Jan-2001.
- [47] M. Gyöngy and C.-C. Coussios, "Passive cavitation mapping for localization and tracking of bubble dynamics," *J. Acoust. Soc. Am.*, vol. 128, no. 4, pp. EL175–EL180, Oct. 2010.
- [48] Lord Rayleigh F.R.S., "XXXI. Investigations in optics, with special reference to the spectroscope," *Philos. Mag. Ser. 5*, vol. 8, no. 49, pp. 261–274, Oct. 1879.
- [49] X. Michalet and S. Weiss, "Using photon statistics to boost microscopy resolution," *Proc. Natl. Acad. Sci. U. S. A.*, vol. 103, no. 13, pp. 4797–4798, Mar. 2006.
- [50] M. D. Gray, E. Lyka, and C. C. Coussios, "Diffraction Effects and Compensation in Passive Acoustic Mapping," *IEEE Trans. Ultrason. Ferroelectr. Freq. Control*, vol. 65, no. 2, pp. 258–268, Feb. 2018.